Numerical modeling of wake capture coefficient in the blade element method for hovering flapping wing

Amir Hossein Zaree [a], Mohammad Hassan Djavareshkian[b,*]

[a,b] Department of Mechanical Engineering, Faculty of Engineering, Ferdowsi University of Mashhad, P.O. Box 91775-1111, Iran

*corresponding author, M.H.Djavareshkian

Abstract:

In this study, models for the wake capture lift and drag force coefficients of a hovering flapping wing were presented using numerical fluid dynamics simulation to improve the blade element theory. The investigated wing is inspired by the fruit fly and has combined flapping and pitching movements. The effect of changing the wing acceleration time at the start ($\Delta\tau_A$) and end of the half cycle ($\Delta\tau_D$), as well as the Reynolds numbers in the range of 136 to 6800, on wake capture using the Taguchi orthogonal array test design, is investigated using the numerical fluid dynamics method, and the values of average lift and drag coefficients due to wake capture are obtained. These force coefficients were applied to linear and non-linear regression methods to obtain the mathematical model, and a model for its changes was extracted. Finally, to obtain the instantaneous coefficients, the extracted models were placed in the normal distribution function, and the final instantaneous model was obtained. Examining the verification cases of the application of these wake capture relationships in the blade element theory, as well as the effects of translational force, rotational force, and added mass force, revealed that this developed theory is capable of correctly predicting the wake capture force's initial peak. The force coefficient trend in the blade element theory results is similar to the CFD results, according to a qualitative examination of the lift and drag force coefficients in a half cycle. This demonstrates a significant result: this theory, which is divided into four parts: transnational, rotational, added mass, and wake capture, adequately covers the general physics of these complex movements and can be widely applied.

Keywords: blade element theory, wake capture, regression, flapping wing

1-Introduction:

In the past few decades, studying insects' aerodynamics to simulate and build them has attracted researchers' attention[1-3]. These researches have included experimental modeling of the wing[1, 4, 5], computational fluid dynamics (CFD)[6, 7], analytical[8, 9] and quasi-steady methods[4, 6, 10-15]. Experimental and CFD simulations are usually time-consuming and expensive. Nevertheless, quasi-steady methods such as improved blade element theory, which have low computational cost, can be used as efficient methods if their accuracy is increased[10]. The accuracy of these methods depends on

precise knowledge of the aerodynamic mechanisms governing insect flight. Among these mechanisms, we can mention delayed stall, circulation caused by wing rotation, added mass effect, and wing and wake interaction effect (wake capture)[10, 11]. Previous research has presented models for three primary mechanisms[11, 14]. However, the effect of wake capture at the beginning of the flapping cycle in insect-like movements has not been included in the blade element theory as a model[11, 13].

The unsteady movement of the wing in flapping flight causes the creation and release of vortices with different structures in the wake[16-18]. Among these vortices, it can be mentioned the leading-edge vortex (LEV), trailing-edge vortex (TEV), wing tip vortex (TV), and wing root vortex (RV)[19]. By itself, there is interference between these vortices at every moment. However, the wing's reciprocating motion causes it to interact with its released vortices in the previous cycle[1, 4, 20]. This phenomenon is known as wing wake interaction or wake capture[1, 11, 19]. Although the effect of wake capture shows itself in the whole wing cycle, its practical effects are often observed at the beginning of the flapping cycle[7, 19, 21, 22]. In their review, Chin and Lentik[23] stated that during the change of wing course, the wing can capture its abandoned wake and recover some of its energy in the fluid. The wing-wake interaction can increase the force generation by increasing the effective speed of the fluid[1, 19]. On the other hand, it can decrease lift production by creating a suction area under the wing [21] or a downwash [22] on it. In general, it can be said that the released vortices strongly depend on wing movements and flow conditions[24, 25], which affect the amount of wake capture effect. Researchers have used experimental[1, 21, 26] and numerical modeling[13, 19] to obtain the amount of force caused by the wake capture effect. Although it is possible to obtain this force in experimental and numerical work, obtaining an expression for the quasi-steady method requires many resources from experimental work or computational fluid dynamics[13]. The section that follows will provide an overview of significant works in this field.

By revealing the flow field around the wing, Dickinson et al.[1] showed that the wing collides with the vortex left in the previous half-cycle at the beginning of the new half-cycle, and this can lead to force generation. Sane and Dickinson[4] stated that the interaction of the wing and the tail, along with the flapping and throwing effect of the wing, can make up to 25% of the total force. Birch and Dickinson [4] showed that the net force for flapping motion for the first flapping cycle (starting from rest) differs from the subsequent cycles, indicating the wake capture effect. Wu and Sun [7] stated that depending on the wing kinematics at stroke reversal (downstroke or upstroke), the wake effect may increase or decrease lift and drag forces at the start of a half-stroke. This is because the wing "impinges" on the spanwise vorticity created during stroke reversal at the start of the half-stroke, and the distribution of the vorticity depends on the wing's kinematics during stroke reversal. Lehman [27] stated that the flow created by the preceding half stroke reduces the effective angle of attack of a single oscillating wing but allows for recycling kinetic energy from the wake via the wake capture mechanism. He noted that during the dorsal stroke reversal in two-winged insects, the acceleration fields created by each wing might interact substantially via the clap-and-fling mechanism. As part of researchers' efforts to

understand the effect of wake capture, Lua et al.[19] discovered that the duration of wing deceleration has a significant effect on wake capture. They showed that as $\Delta\tau_D$ decreases at the end of the half cycle, the lift and drag force coefficients increase at the beginning of the next half cycle. They also showed that with the change of $\Delta\tau_A$, there is no significant change in the average force coefficients in the indicated intervals in each cycle. However, reducing acceleration duration resulted in an earlier wake capture peak. Lee and Lua [28] observed a considerable wake capture impact on a two-dimensional (2-D) wing subjected to a simple harmonic hovering motion (SHM) in terms of magnitude. However, they found no indication of considerable wake capture in their investigation of three-dimensional (3-D) wings performing SHM. They also showed an improvement in the average result due to the wing-wake interaction decreasing rapidly with the addition of 3D effects. Their results stated that for wings similar to natural insects (low aspect ratio and low Rossby number), the effect of wing-wake interaction has a slight improvement in the speed and a slight increase in energy consumption. However, their results were obtained according to simple harmonic motion, and hovering insect-like motion with rapid changes during the end of stroke was not investigated in their research. They remarked that the duration of the deceleration may be a crucial factor in influencing the magnitude of the wake captured by 3-D flapping wings.

In 2018, Ado Akuto et al. [26, 29] investigated the effect of aspect ratio on wing-wake interaction during the half-cycle change in the range of Reynolds 10000 using an experimental test platform. Their results showed a jet-like flow induced by a pair of trailing edge vortices in the opposite direction is created. They found that the wing-wake interaction that happens at the root of the wing is different from the one that happens at the tip of the wing. Also, their observations showed that the presence of two pairs of trailing edge vortices leads to the creation of a strong flow towards the lower surface of the wing and causes an impact on the lift force. They pointed out that although the usual wing-wake interaction occurs on the tip of the wing, a different phenomenon of wing-wake interaction appears on the trailing edge and wing root side, which is more evident at low aspect ratios and, regardless of the length of pitching motion of the wing, causes a force peak.

In 2020, Lee et al.[30] investigated the parameters and functions of the wing speed during the stroke reversal time using the immersed boundary Lattice Boltzmann method. They studied the wing under flapping motion without pitching and investigated the effects of changing the flapping amplitude and the duration of stroke reversal. They showed that stroke reversal duration affects the remaining vortices in the wake. They observed the effect of increased force due to the wake capture at the beginning of the new stroke and showed that the duration of the stroke reversal affects the moment when the wake capture occurs.

Hu et al.[13] in 2020, to import the wake capture effect into the blade element theory, moved the wing under SHM through computational fluid dynamics simulations for flapping and pitching. By applying this movement, they observed the wing-wake interaction in the middle of the half-cycle. They introduced the difference in the lift and drag force coefficient of the first and fifth half cycles as the

effect of the wake capture as a fitted function similar to the translational force in the general quasi-steady modeling. However, in non-SHM, their model cannot account for the effect of increasing force at the start of the stroke.

Altogether, in recent years, the blade element theory has been regarded as a quick way of modeling the flapping wing, with researchers favoring its increased accuracy. As many of the mechanisms included in the flapping wing, such as the delayed stall effect, additional mass force, rotational force, and wake capture effect, are correctly anticipated, the accuracy of blade element theory improves. However, because of the complexity of the flow during wake capture, one of the recent challenges for researchers has been the isolation of this effect [11, 19]. The literature review shows that the effect of negative acceleration of the wing ($\Delta\tau_D$) on the wake capture modeling has not been included in the blade element theory. Therefore, providing a suitable model for these forces can improve the blade element theory.

In general, this paper aims to improve the performance of the blade element theory for simulating the simultaneous movement of flapping and pitching in the hovering flight of an insect wing. The literature review shows that wake capture modeling at the beginning of the new stroke has not been included in the blade element theory. In this research, to improve the performance of the blade element theory to predict the lift and drag coefficients, the wake capture effect is entered as a model for it. In this way, the effect of the three parameters of acceleration duration($\Delta\tau_A$), deceleration duration($\Delta\tau_D$), and *Re* is considered. In the following, by using nonlinear regression, the models according to the mathematical functions provided and, finally, by using the normal distribution functions, relations for the instantaneous lift and drag coefficients of the wake capture are presented for improvement of the blade element theory results.

2- Basics of the unsteady blade element method

In the blade element theory method, to obtain the final forces, first, the wing plane is divided into a certain number of elements. Finally, according to the kinematics of the wing, the forces acting on each element are obtained and integrated over the entire wing surface, and the wing's instantaneous force is obtained [31, 32]. The translational forces are introduced as the basic forces at each moment due to the wing's instantaneous angle of attack. The added mass force due to the wing acceleration and the rotational force that occurs due to the rotation rate of the wing around the pitch axis is included as additional unsteady effects. In the continuation of this section, all three translational, added mass, and rotational forces involved in the overall output force of the blade element theory are introduced.

Figure 1 shows the wing with a length of *R* that is divided into certain elements with a width of *dr*. A specific wing element's cross-section is placed at a distance *r* from the wing root and is shown as a strip with a width of dr. An orthogonal coordinate system, *OXYZ*, describes the flapping motion. The *Z* axis is the flapping axis, and the *XY* plane is the flapping stroke plane. ξ is the pitch axis of the wing, and its position is determined by ψ angle relative to the *X*-axis. The mentioned movement represents the flapping motion. In addition to this flapping motion, the wing can rotate around the pitch axis [31]. The

η axis is tangential to the flapping motion, and ζ is perpendicular to the stroke plane and $\xi\eta\zeta$ is local coordinate system of the flapping wing. Figure 2 shows the translational forces of the wing section with chord length $c(r)$ and width dr in the local coordinate system. V_T is the total speed of the flow caused by the flapping motion, and the angle of attack α is the angle between the wing chord and the total speed. The lift and drag forces acting on the section are shown by dL and dD, respectively.

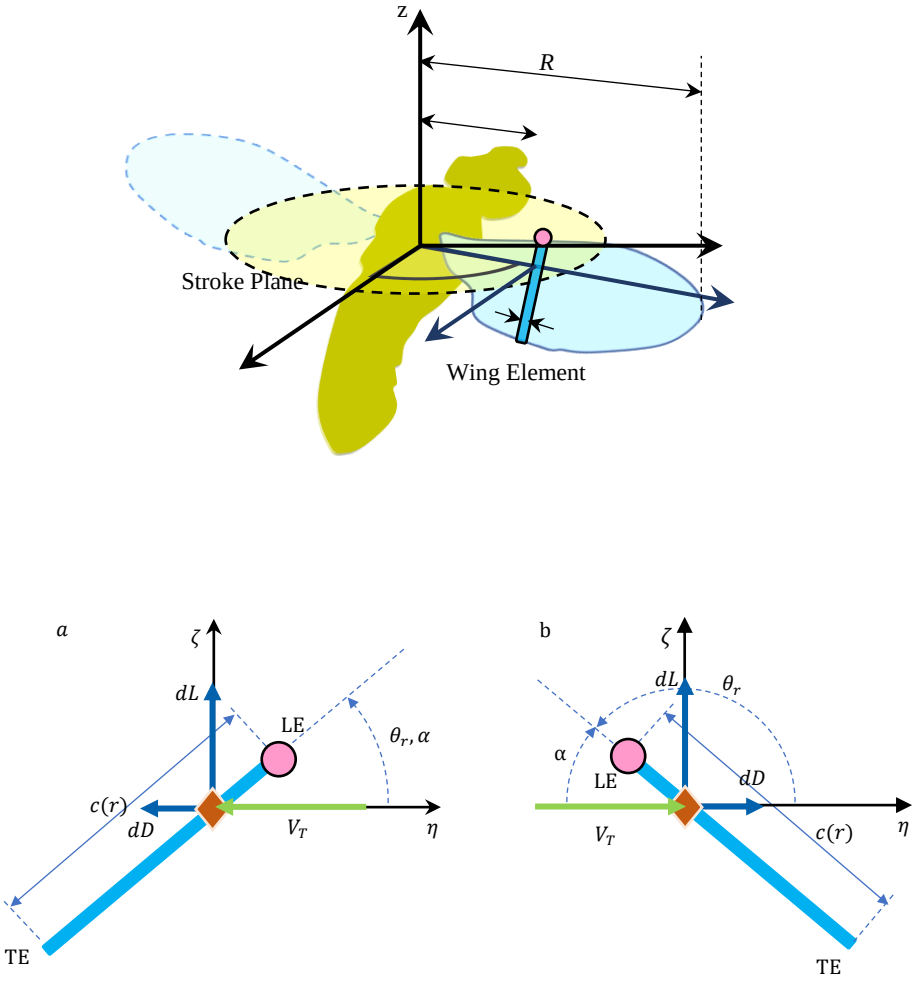

Figure 2: A view of a cross section of a blade element and definition of variables

At each wing section, the lift and drag forces acting on that section are calculated and added up along the entire wing length, and the wing's overall lift and drag forces are obtained[7]. These forces are along the η and ζ axes, which are the directions of the axial force and the overall lift force, respectively, are calculated by relations (1) and (2):

$$dL = \frac{1}{2}\rho {V_T}^2 C_l dS \quad (1)$$

$$dD = \frac{1}{2}\rho {V_T}^2 C_d dS \quad (2)$$

Where ρ is the fluid density, C_l and C_d are the lift and drag translational coefficients and $dS = c(r)dr$ is the wing's element area. The translational lift and drag forces at a given point are determined by integrating equations (1) and (2) in the wing span direction. Lee et al. [11] presented a model for translational force coefficients using computational fluid dynamics results. They obtained the translational coefficients in terms of Reynolds number according to relations (3) and (4). They also explored the coefficients' sensitivity to the aspect ratio AR and the Rossby number $Ro = \frac{R}{\bar{c}}$. They offered the corrections for f_{AR} and f_{Ro} based on the relationships (5) and (6). These models are employed as translational force models in the current work.

$$C_l(\alpha) = (1.966 - 3.95Re^{-0.429})\, sin\, 2\,\alpha \tag{3}$$

$$C_d(\alpha) = (0.031 + 10.48Re^{-0.764}) + (1.873 - 3.14Re^{-0.369})(1 - cos\, 2\,\alpha) \tag{4}$$

$$f_{AR} = 32.9 - 32.0AR^{-0.00361} \tag{5}$$

$$f_{Ro} = -0.205 \arctan[0.587(Ro - 3.105)] + 0.870 \tag{6}$$

The added mass force is one of the unsteadiness of flow physics in the flapping wing aerodynamic mechanism. Knowing this force and obtaining its value will improve the quasi-steady methods in flapping wings. It is assumed that the surrounding fluid affecting the wing is the disk with the element's chord diameter $c(r)$ and the thickness *dr*. The mass of the fluid disk is equal to $\pi/4\,\rho c(r)^2 dr$, and if the acceleration of the reference point on the wing element is equal to a_n, the added mass force on the wing element is obtained from equation (7)[10]. a_n is also determined using equation (8), where $x_m = x_r - x_f$ is the distance between the reference point and the wing's axis of rotation. x_f is the distance between the leading edge and the wing element's pitching axis, and x_r is the distance between the leading edge and the reference point considered to be half the chord length of each element[10].

$$dF_A = -\frac{\pi}{4}\rho c(r)^2 a_n dr \tag{7}$$

$$a_n = x_m\ddot{\theta}_r + r\ddot{\psi}\, sin\, \theta_r + x_m\dot{\psi}^2\, cos\, \theta_r\, sin\, \theta_r \tag{8}$$

Rotational force occurs due to the rotation rate of the wing around the wing axis. Figure 3 shows a wing cross-section with rotational and translational speed around the wing axis. Without skin friction, the rotational force is applied perpendicularly to the wing section[10]. Finally, after imaging the force along the local axes, the rotational force on the wing elements is integrated into the wing spanwise direction and is obtained at every moment. Van Veen et al. [33] presented a general model for predicting rotational forces by simulation based on the immersed boundary method. To propose their model, they used an elliptical wing placed in six different positions of the twist axis along the wing's chord. They also simulated two wing models of fruit-fly and malaria mosquito. They used a combined model based

on the theory of Kutta-Joukowski[1] and the rotational drag model[34]. To obtain a general model, they proposed the force $F_{\text{stroke}-\text{pitch}}$, which is produced in the combined rotational and translational motions, is proportional to the pitch–stroke coupled second-moment-of area $\sqrt{S_{xx}S_{yy}}$. They also suggested that the force F_{pitch}, which is only caused by the pitching of the wing, is proportional to the asymmetric second-moment-of-area $S_{x|x|}$. Finally, they showed that with these assumptions, a general model for rotational force could be considered according to relations (9) and (10). This model has a constant coefficient $C_{rot} = 2.08 \pm 0.13$ for both $F_{\text{stroke}-\text{pitch}}$ and F_{pitch} forces.

$$F_{rot} = F_{\text{stroke}-\text{pitch}} + F_{\text{pitch}} \tag{9}$$

$$F_{rot} = C_{rot}\rho\left(\sqrt{S_{xx}S_{yy}}\dot{\psi}\dot{\theta}_r + S_{x|x|}\dot{\theta}_r^2\right); \quad \sqrt{S_{xx}S_{yy}} = \sqrt{\int x^2 dS \int y^2 dS}\ ;\ S_{x|x|} = \int x|x|dS \tag{10}$$

To apply the rotational force model proposed by Van Veen et al. in the blade element theory, the values of $\sqrt{S_{xx}S_{yy}}$ and $S_{x|x|}$ for the presented simulation, equal to $2.6574\times10^{-4}\,\text{m}^4$ and $-0.5223\times10^{-4}\,\text{m}^4$, respectively, have been calculated.

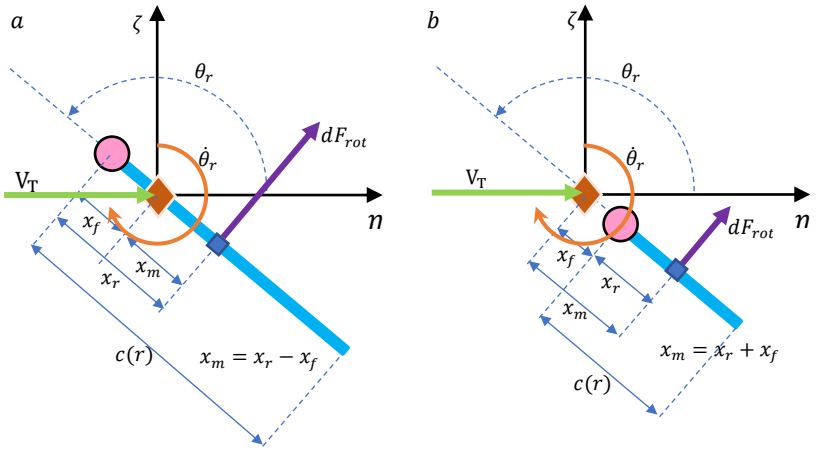

Figure 3. Rotational force applied to the wing section

3- Improving the unsteady blade element method

As mentioned in the previous sections, the conventional blade element theory includes three parts: transfer, added mass, and rotation, and it is not able to predict the force caused by the capture of the trail released from the previous cycle in the new cycle. In the current work process, to calculate this effect and improve this theory, the following process is performed: 1-Selection of three parameters $\Delta\tau_A$, $\Delta\tau_D$, and *Re* as independent parameters affecting the wake capture. According to Lua et al.'s study, wing acceleration's effect at the beginning and end of the half-cycle and Reynolds influence the wake

capture values. In addition, other parameters such as wing shape, wing pitching, and flapping kinematics can also be effective. Due to the limitations of computational costs, only three parameters $\Delta\tau_A$, $\Delta\tau_D$, and *Re*, are investigated in the current work. 2-Designing the CFD experiment using the Taguchi orthogonal array method. The Taguchi orthogonal array table $L_{18}(6^1\times3^2)$ has been used to reduce the number of runs, shown in Table 1. The total number of tests equals 18, and three levels are considered for two parameters $\Delta\tau_A$and $\Delta\tau_D$ and six levels for Re. According to the previous work, levels of two parameters $\Delta\tau_A$and $\Delta\tau_D$were considered in the logical range of 0.06 to 0.18. The Reynolds levels were selected according to the range of common insects. Since, according to the previous studies, the changes of aerodynamic coefficients were constant in the range of 136 to 6800 from one Reynolds onwards, there was a need for more levels for Reynolds to be able to capture the changes of the wake capture. The level value of each parameter is shown in Table 1. It should be noted that if all permutations between levels were considered, 54 tests would be needed. To model the effect of trail capture, the Reynolds number of the flow was considered in the range of 136 to 6800 in two regimes, laminar and turbulent, and for both regions, the flapping motion was simulated with the twisting of the wing, and the aerodynamic forces were performed by the method numerical fluid dynamics based on finite volume was performed in Fluent software. Then, using the CFD output, the effect of wake capture is calculated, and regression is used to obtain the desired functions. The obtained functions of the three input parameters are entered into another time distribution function to enter the blade element theory at each moment. Figure 4 depicts the flowchart of the process used in the current work.

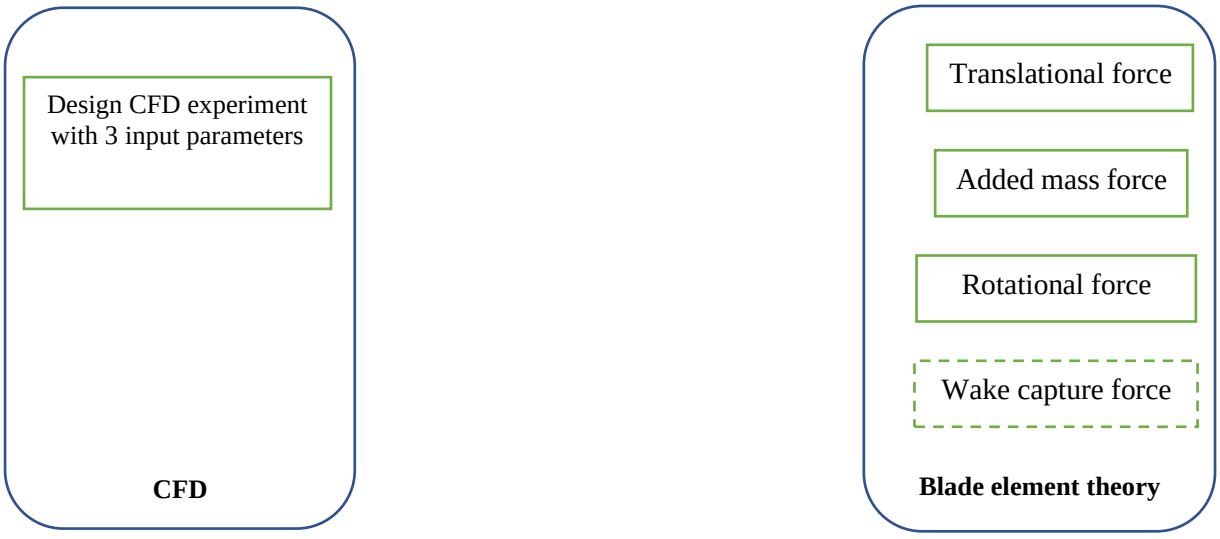

Figure 4. Algorithm of the process performed in the current work

Table 1. Input parameters and level values of each of them

Dimensionless parameter	Level 1	Level 2	Level 3	Level 4	Level 5	Level 6
Re	136	272	680	1360	2720	6800
$\Delta\tau_D$	0.06	0.12	0.18	-	-	-
$\Delta\tau_A$	0.06	0.12	0.18	-	-	-

Table 2. Taguchi orthogonal array $L_{18}(6^1\times3^2)$

Test number	*Re*	$\Delta\tau_D$	$\Delta\tau_A$	Test number	*Re*	$\Delta\tau_D$	$\Delta\tau_A$
1	1	1	1	**10**	4	1	3
2	1	2	2	**11**	4	2	1
3	1	3	3	**12**	4	3	2
4	2	1	1	**13**	5	1	2
5	2	2	2	**14**	5	2	3
6	2	3	3	**15**	5	3	1
7	3	1	2	**16**	6	1	3
8	3	2	3	**17**	6	2	1
9	3	3	1	**18**	6	3	2

4-Geometric features of the studied wing:

A wing model of a fruit-fly insect (Figure 5) that was inspired by Lua et al. [19] study was used to simulate, compare, and examine the wake capture effect on instantaneous lift and drag force coefficients. Table 1 shows the geometric properties of the wing. The density of the fluid is set to 1229 Kg/m^3 [19].

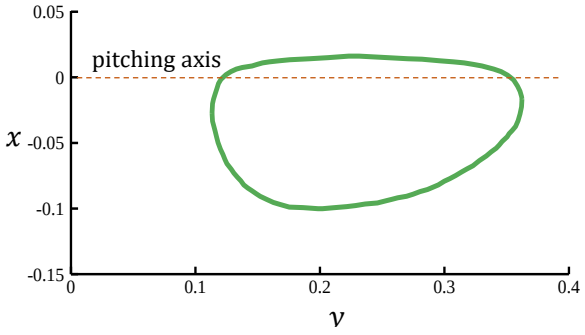

Fig.5: Wing plan along with the position of pitching axis

Table 3: Wing Geometric Properties [۱۹]

value	symbol	Geometric feature
0.3631 m	R	Wing length
0.0929 m^2	$\bar{c}$	Mean wing chord
0.25 m	b	Span
0.2394 m	R_g	Radius of gyration
0.02296 m^2	S	Wing area
2.69	AR	Aspect ratio

Figure 6 shows the movement characteristics of the flapping and pitching angles in terms of dimensionless time in the downstroke. Figure 6 (a) shows the movement of a cross-section in a complete flapping course, including the downstroke and upstroke. Figure 6 (b) also shows the curve of the angles, speeds, and angular accelerations of flapping and pitching motion, along with the change of the angle of attack in the downward course. The ratio of flapping speed to maximum speed, the velocity at the wing gyration radius (V_{max,R_g}), is equal to 0.1905 m/s. The sweeping angle of the wing in a one-half cycle is 155 degrees, and the angle of attack in the middle of each half cycle also reaches a limit value of 40 degrees. Relations (11) and (12) have been used to calculate the lift and drag coefficients of the blade element, which are indicated by C_L and C_D, respectively. In these relationships, S is the total surface of the wing.

$$C_L = \frac{L}{0.5\rho V_{max,R_g}^2 S} \tag{11}$$

$$C_D = \frac{D}{0.5\rho V_{max,R_g}^2 S} \tag{12}$$

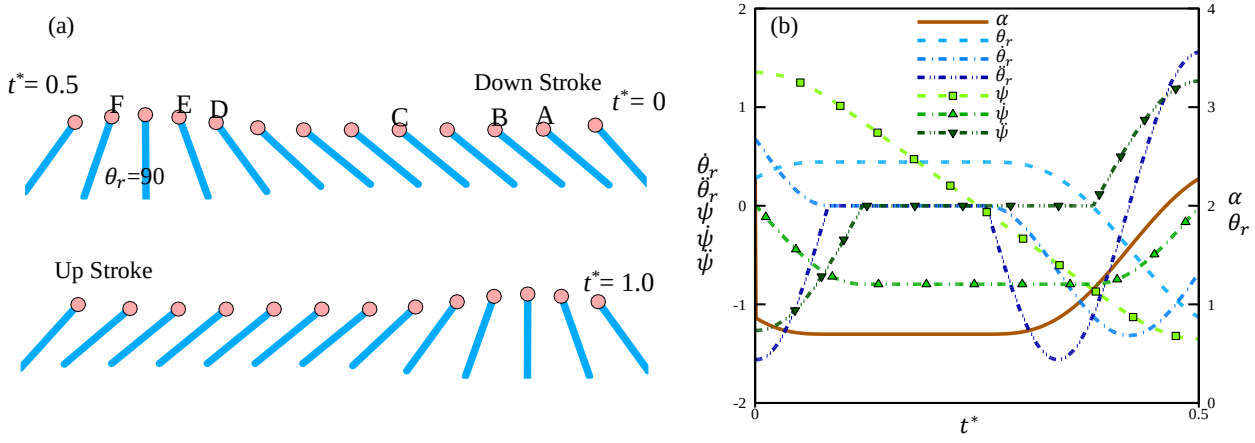

Fig.6: wing kinematic parameters curves: a: schematics of wing cross section in a flapping cycle b: angels, velocities and angular accelerations

6- Numerical method and validation

In this research, the solution of the Navier-Stokes equations has been used for the numerical simulation of computational fluid dynamics. The fluid's governing equations are continuity and momentum equations in three directions according to relations (13) and (14).

$$\boldsymbol{\nabla}.\boldsymbol{u} = 0 \tag{13}$$

$$\rho\frac{D\boldsymbol{u}}{Dt} = -\boldsymbol{\nabla}p + \mu\nabla^2\boldsymbol{u} \tag{14}$$

Where u is the velocity vector in the reference coordinate system, ρ is the fluid density, p is the pressure, and μ is the dynamic viscosity. For simulation, Ansys-Fluent 19.3 commercial software was used. To solve the equations, the second-order discretization of spatial and temporal terms has been used. However, due to the flow Reynolds number range from 136 to 6800, the $k-\omega$ turbulence model with an additional intermittency equation for the transition regime has been used. This method is called SSTI and uses an additional equation for flow intermittency to enable the $k-\omega$ model to model laminar to turbulent transition. The results of the experiments have been well matched by this model in the aerodynamic simulation of the vertical axis wind turbine, which is accompanied by wind turbine-like phenomena such as dynamic stall [35].

Flapping and pitching movements are implemented using the sliding mesh approach. Meshing for simulation is done using two spherical regions, inner and outer. The wing is inside the inner zone and this zone slides into the outer zone. Figures 7 show a schematic of these areas as well as the sample wing. The diameter of the external calculation area was determined to be 6 meters based on the independence results (about 65 times the average chord). Furthermore, the inner area has a diameter of 0.55 meters. The boundary condition of no slip on the wing wall is considered and the external boundary condition is also set to zero relative pressure. The prism grid type surrounds the wing of the boundary layer, and the rest of the volume is tetrahedral. The surface grid on the wing is triangular as well. The highest mesh skewness is 0.79, and the lowest mesh quality is 0.2. The height of the first grid is equal to $\bar{c}/90$, and the expansion ratio is assumed to be 1.1. In the worst-case scenario, the y+ with this condition is less than 10. Figures 8, and 9 depict the results of grid independence and time step in each period. According to these results, the grid with the numbers 1.6 million, and 1000-time steps in each cycle is considered. Figure 10 shows the results of published [19] and simulated drag and drop coefficients. The force coefficients and the difference between the sixth and first cycles, as shown in this figure, are in good agreement with the published CFD study.

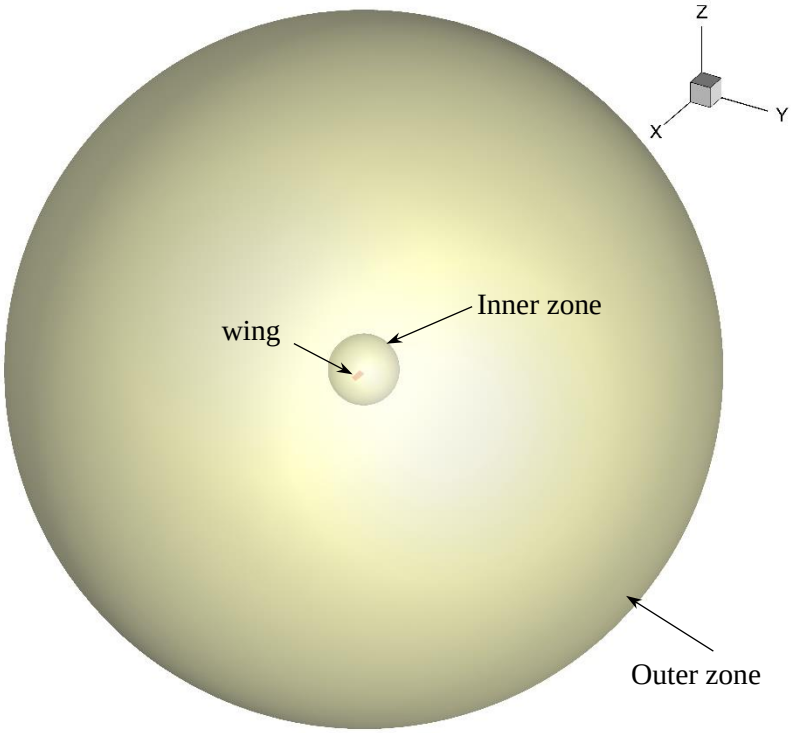

Fig.7: Inner and outer zones for sliding mesh method

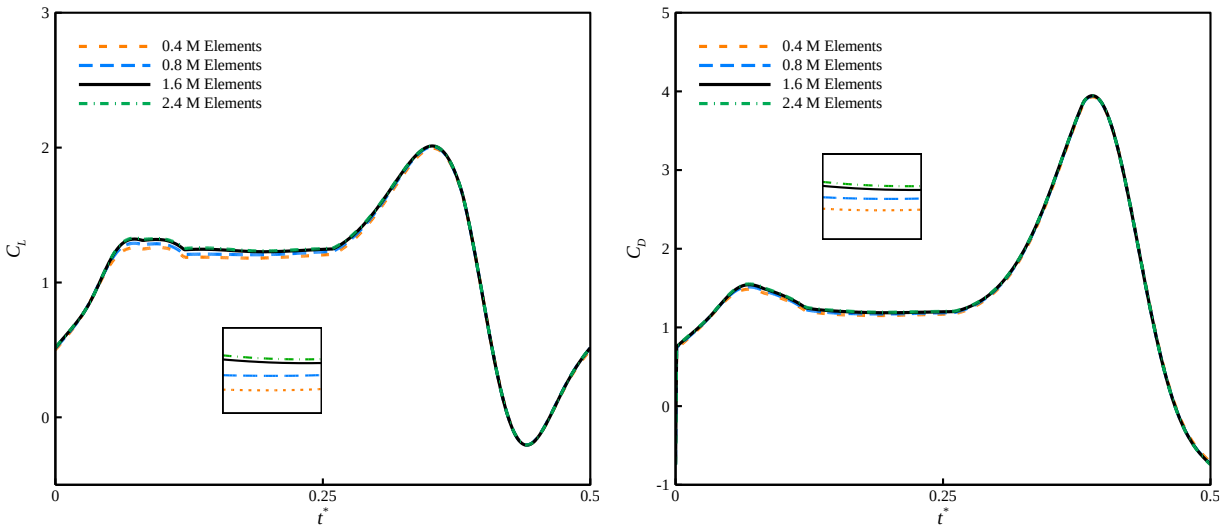

Fig.8: Mesh independency

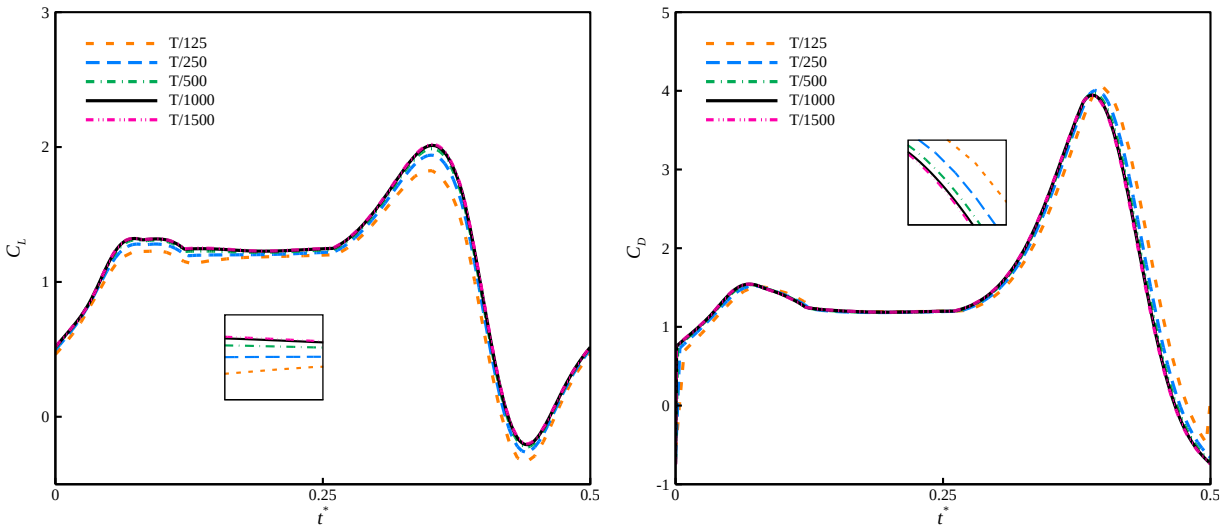

Fig.9: The results of time step independency

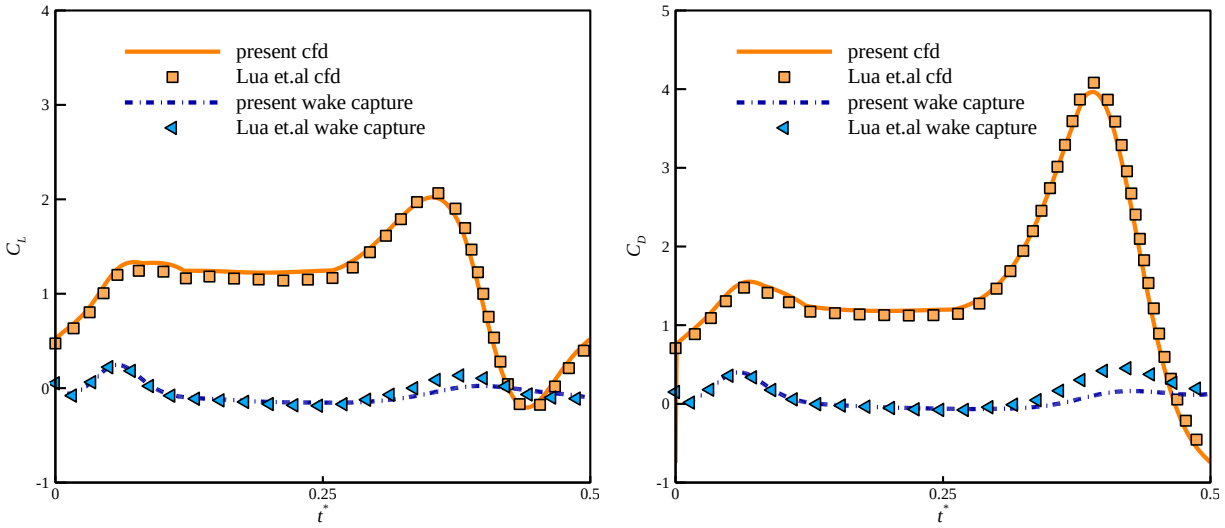

Fig.10: Validation of force coefficients with published data[19]

7- Results and discussion

In each CFD run, the instantaneous wake capture effect is calculated by subtracting the average of the eighth to tenth cycle lift and drag coefficients from the first cycle. Figure 11 depicts the lift and drag coefficients in the first and tenth cycles, as well as the difference between these cycles as the effect of wake capture, for Run No. 2. The wake capture effects of ΔC_L and ΔC_D can be seen in this figure as a peak in the difference of the coefficients in the initial time of the half cycle. This force difference occurred almost in the range of 0.1 dimensionless times and was averaged in this range, as shown in table 4 for the lift and drag coefficients with $\overline{\Delta C_L}$ and $\overline{\Delta C_D}$ respectively. In addition, the dimensionless time corresponding to the occurrence of the maximum of ΔC_L and ΔC_D is marked with a μ^* in this table.

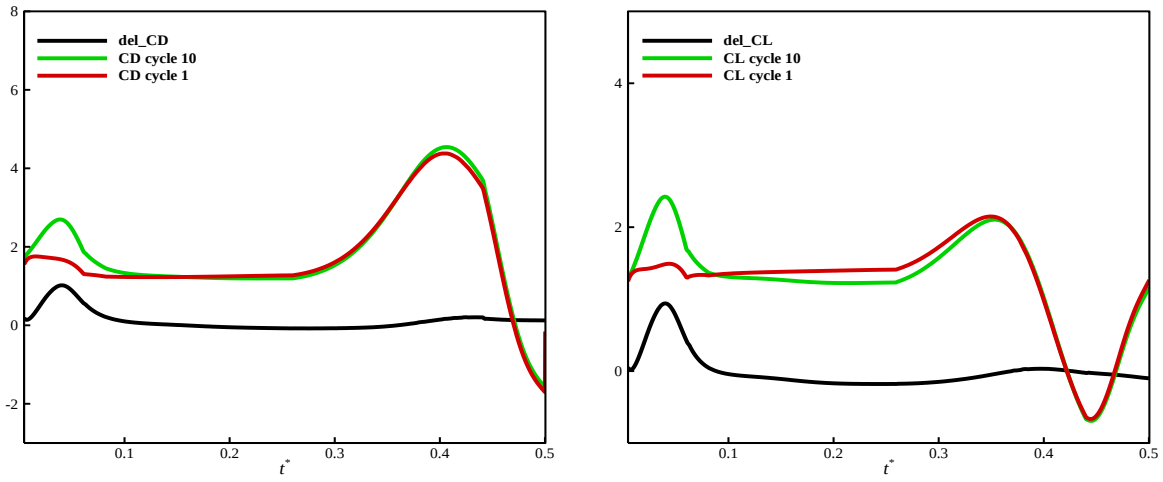

Fig.11: Lift and drag coefficients of cycles 1 and 10, as well as the difference between them.

Table.4: numerical results of the average of lift and drag coefficients and dimensionless time corresponding to the maximum of them

Test number	$\overline{\Delta C_L} \pm S.D$	$\overline{\Delta C_D} \pm S.D$	μ^*	Test number	$\overline{\Delta C_L} \pm S.D$	$\overline{\Delta C_D} \pm S.D$	μ^*
1	0.380±0.003	0.510±0.003	0.040	**10**	0.505±0.008	0.479±0.006	0.055
2	0.102±0.002	0.234±0.002	0.058	**11**	0.307±0.004	0.325±0.003	0.041
3	0.033±0.002	0.146±0.002	0.068	**12**	0.107±0.015	0.141±0.017	0.047
4	0.475±0.004	0.539±0.003	0.039	**13**	0.559±0.005	0.535±0.004	0.051
5	0.177±0.002	0.249±0.002	0.059	**14**	0.237±0.006	0.237±0.005	0.068
6	0.080±0.001	0.151±0.001	0.066	**15**	0.161±0.010	0.188±0.013	0.036
7	0.510±0.002	0.519±0.001	0.052	**16**	0.535±0.002	0.489±0.002	0.059
8	0.211±0.002	0.235±0.001	0.065	**17**	0.347±0.026	0.351±0.002	0.031
9	0.114±0.007	0.172±0.002	0.033	**18**	0.150±0.010	0.160±0.009	0.040

Instead of calculating all possible models, the Taguchi method only calculates a few typical models following the orthogonal array[36, 37]. Finding the best possible combination of factors is the goal of the Taguchi method[38]. This method uses the SNR (signal-to-noise ratio) as an objective to measure the performance variability of the chosen factors. The SNR is used to determine which factor levels are preferable. In the analysis of the SNR, there are three different types of performance characteristics: the lower-the-better, the higher-the-better, and the nominal-the-best[38, 39]. In this study, the larger, the better analysis is used to calculate the SNR ratio and determine the sensitivity of factor levels using equation 15.

$$SNR = -10\log\left(\frac{\sum_j \frac{1}{Y_j^2}}{n}\right) \quad (15)$$

Where Y_j denotes the number of responses for the given factor-level combination and n denotes the number of responses in the factor-level combination (where n is equal to one). Figures 12, 13, and 14 show the effect of each parameter $\Delta\tau_A$, $\Delta\tau_D$, and *Re* on $\overline{\Delta C_L}$, $\overline{\Delta C_D}$, and μ^* using Taguchi analysis of signal-to-noise value respectively. As can be seen, the effect of *Re* on $\overline{\Delta C_D}$ is less than that of $\overline{\Delta C_L}$. It can also be seen in Figure 14 that the parameters $\Delta\tau_A$, *Re*, and $\Delta\tau_D$, respectively, have the greatest effect on μ^*.

Fig.12: Signal to noise ratio in terms of

7-1 Regression analysis

To obtain the final model for each of the dependent variables $\overline{\Delta C_L}$ and $\overline{\Delta C_D}$ and μ^* , regression analysis has been used and the best model is suggested. For this purpose, linear models were evaluated first. For the dependent variables of the response $\overline{\Delta C_L}$ and $\overline{\Delta C_D}$, the second-order linear model with complete sentences according to equation 16 was considered. Because the Reynolds variable has a range of long changes and large numbers, the ln function was used to reduce this range to smaller numbers. Using this function changes the range of the ln R_e between 4.91 and 8.82.

$$RESP = \beta_0 + \beta_1 \ln(Re) + \beta_2 \Delta\tau_D + \beta_3 \Delta\tau_A + \beta_4 \ln(Re)\Delta\tau_D + \beta_5 \ln(Re)\Delta\tau_A + \beta_6 \Delta\tau_D \Delta\tau_A + \beta_7 (\ln(Re))^2 + \beta_8 {\Delta\tau_D}^2 + \beta_9 {\Delta\tau_A}^2 + \varepsilon \quad (16)$$

The prediction model was created using Minitab 20.4 software. Until all the sentences with the proper significance level are reached, the model is developed using a stepwise algorithm of linear regression in the Minitab software[40-42]. The manual for this software[43] contains information on the stepwise algorithm and how to choose it. Additionally, non-linear regression models were examined using several suggested prediction functions, and finally, the best model was chosen. The most similar functions were chosen for the proposed functions based on the form of changes of the variables in terms of each other[44]. In general, the following factors are taken into account when selecting the best model: 1. All of the sentences in the proposed model have a significant contribution, and the sentences with a low level of significance have been removed. 2. The model's standard error S should be small enough. 3. The residual analysis graphs should show a suitable trend. Relationships 17–19 depict the obtained models for $\overline{\Delta C_L}$ and $\overline{\Delta C_D}$ and μ^*, respectively. The final regression model for $\overline{\Delta C_L}$ and $\overline{\Delta C_D}$ is obtained using non-linear regression, and the exponential prediction function for these parameter changes in terms of Reynolds is chosen. The standard error *S* (non-relative error) of each model for $\overline{\Delta C_L}$ and $\overline{\Delta C_D}$ is equal to 0.0345 and 0.0355, respectively, and it shows suitable values based on the range of their changes in Table 4. The final regression model for μ^* is also obtained using second-order linear regression modelling with fewer sentences than the model in equation 16. This model's standard error *S* is equal to 0.00408 of the dimensionless time t^*, indicating a reasonably suitable range.

$$\overline{\Delta C_L} = 0.94839 - 0.195478 \exp(-0.00234646 Re) - 7.9318 \Delta\tau_D + 19.6205 {\Delta\tau_D}^2 \quad (17)$$
$$S = 0.0345025$$

$$\overline{\Delta C_D} = 0.903189 - 0.0356281 \exp(-0.00027928 Re) - 7.18999 \Delta\tau_D + 17.7339 {\Delta\tau_D}^2 \quad (18)$$
$$S = 0.0354756$$

$$\mu^* = 0.04195 - 0.002684 \ln(Re) - 0.2236 \Delta\tau_A + \varepsilon \quad (19)$$
$$S = 0.0040837$$

The normal distribution residuals analysis chart is used to determine the statistical significance of coefficients in prediction models. If this graph shows a straight line, it indicates that the model's residual errors are normally distributed and the coefficients are significant[39]. Figures 15, 16, and 17 show this chart for each of the $\overline{\Delta C_L}$ and $\overline{\Delta C_D}$ and μ^* models, respectively. As seen in these figures, the residuals are close to the straight line, demonstrating the appropriateness of their normal distribution.

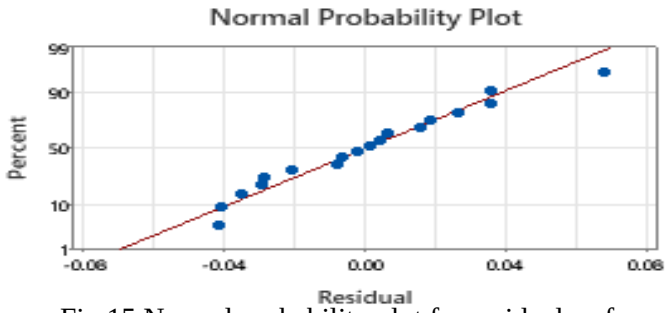

Fig.15 Normal probability plot for residuals of

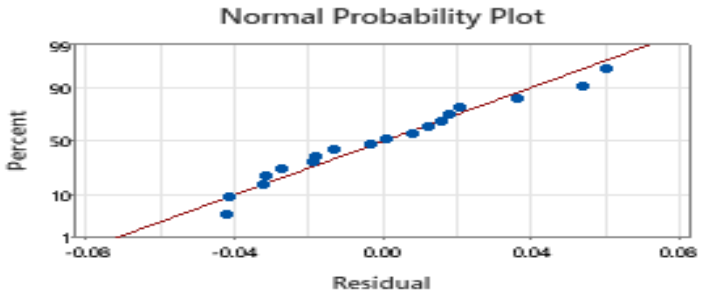

Fig.16: Normal probability plot for residuals of

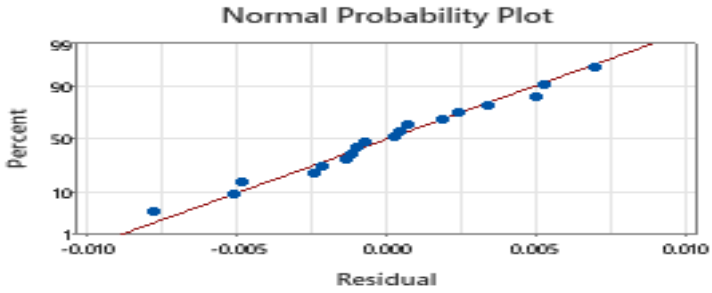

Fig.17: Normal probability plot for residuals of

Figure 18 depicts a graph comparing the fitted values with the numerical results for three variables $\overline{\Delta C_L}$, $\overline{\Delta C_D}$, and μ^* to assess the model's accuracy. As can be seen, all three models predict the numerical results accurately. To test the significance of the model's behavior by changing the independent variables, the contours of the dependent variables $\overline{\Delta C_L}$, $\overline{\Delta C_D}$, and μ^* are shown in figures 19, 20, and 21, respectively. As can be seen in these figures, the contours $\overline{\Delta C_L}$ and $\overline{\Delta C_D}$ increase with increasing Reynolds and decreasing $\Delta\tau_D$, indicating an expected trend. Also, μ^* contour has a consistent shape and changes as Re and $\Delta\tau_A$ change. There is no evidence of physical discontinuity in the contours as the independent variables change.

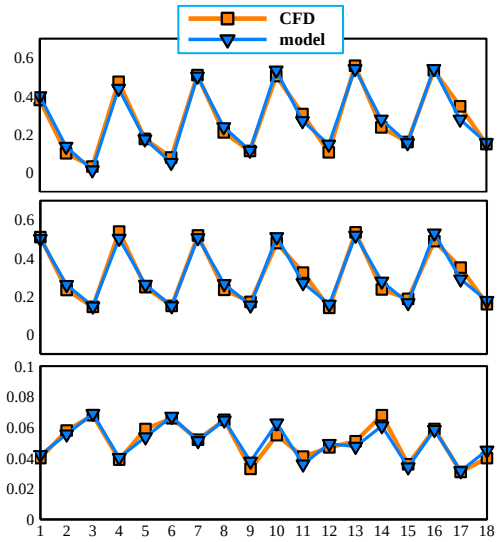

contour of

Fig.20: Contour plot of

contour of μ^*

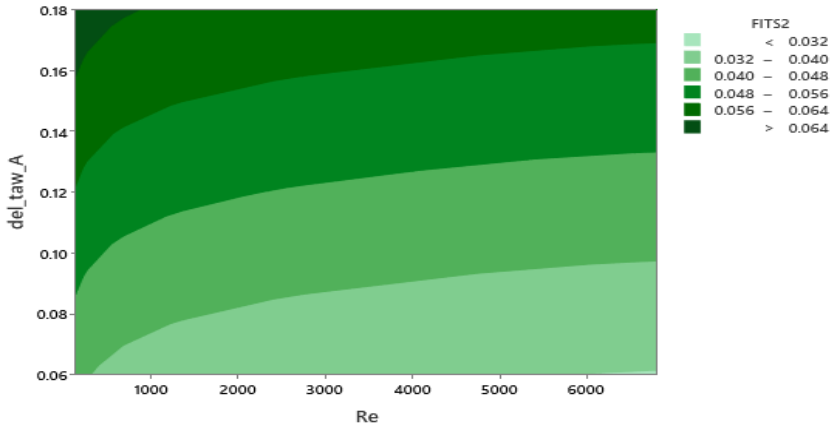

Fig.21: Contour plot of

To verify the regression models, 4 random numerical fluid dynamics executions were performed in different conditions with 18 data used in the models and $\overline{\Delta C_L}$ and $\overline{\Delta C_D}$ and μ^* corresponding to each are shown in Table 5. As can be seen, the relevant models have low errors that are in the range or less than the standard errors of the models, indicating the model's validity in these conditions.

Table5: Comparison of CFD result with regression fitted values of $\overline{\Delta C_L}$, $\overline{\Delta C_D}$ and $\mu^*$for verification tests

Test number	*Re*	$\Delta\tau_D$	$\Delta\tau_A$	$(\overline{\Delta C_L})_{\text{CFD}}$	$(\overline{\Delta C_L})_{\text{model}}$	Difference
V1	272	0.06	0.09	0.45497	0.43986	-0.01511
V2	408	0.03	0.12	0.64064	0.65305	0.01241
V3	1360	0.12	0.12	0.24763	0.27107	0.02344
V4	5440	0.06	0.12	0.57185	0.54312	-0.02874
Test number	*Re*	$\Delta\tau_D$	$\Delta\tau_A$	$(\overline{\Delta C_D})_{\text{CFD}}$	$(\overline{\Delta C_D})_{\text{model}}$	Difference
V1	272	0.06	0.09	0.50762	0.50261	-0.00501
V2	408	0.03	0.12	0.63931	0.67166	0.03235
V3	1360	0.12	0.12	0.26854	0.27139	0.00284
V4	5440	0.06	0.12	0.53883	0.52783	-0.01100
Test number	*Re*	$\Delta\tau_D$	$\Delta\tau_A$	$(\mu^*)_{\text{CFD}}$	$(\mu^*)_{\text{model}}$	Difference
V1	272	0.06	0.09	0.04600	0.04703	0.00103
V2	408	0.03	0.12	0.05500	0.05265	-0.00235
V3	1360	0.12	0.12	0.05100	0.04942	-0.00158
V4	5440	0.06	0.12	0.0500	0.04570	-0.00430

7-2 Obtaining the instantaneous wake capture force coefficients $(C_L)_{WC}$ and $(C_D)_{WC}$

As shown in the figures of the instantaneous wake capture effect distribution of lift and drag force coefficients, this effect begins at a low value, rises to a high point, and then falls back. According to this change process, it is suggested that the normal distribution function be used to model these coefficients in the current work using equation 21. Figure 22 depicts the general process of this equation, which distributes the unit surface value along 6σ on the horizontal axis. Similarly, if $f(x)$ is a normal distribution function, relation 22 holds for any non-unit value of the surface under its graph ($\int_{-\infty}^{\infty} f(x)dx$). Also, By changing μ, the peak of the function along the horizontal axis can be shifted. Because the wake capture coefficients' maximum peak occurs in μ^*T, the entire distribution of this effect is assumed to occur in $2\mu^*T$, and thus $\sigma = 2\mu^*T/6$. Now, assuming the normal distribution of the instantaneous wake capture effect over a range of $0.1T$, equation 24 for $(C_L)_{WC}$ is obtained. Similarly, relation 25 is calculated for the $(C_D)_{WC}$based on regression models $\overline{\Delta C_L}$, $\overline{\Delta C_D}$, and μ^* (relations 17, 18, and 19).

$$f(x) = \frac{1}{\sigma\sqrt{2\pi}} e^{-\frac{1}{2}\left(\frac{x-\mu}{\sigma}\right)^2} \quad (20)$$

$$f(x) = \frac{\int_{-\infty}^{\infty} f(x)dx}{\sigma\sqrt{2\pi}} e^{-\frac{1}{2}\left(\frac{x-\mu}{\sigma}\right)^2} \quad (21)$$

$$\overline{\Delta C_L} = \frac{\int_0^{0.1T}(C_L)_{WC}dt}{0.1T} \Rightarrow \int_0^{0.1T}(C_L)_{WC}dt = 0.1\overline{\Delta C_L}T \quad (22)$$

$$(C_L)_{WC} = \frac{\int_0^{0.1T}(C_L)_{WC}dt}{\sigma\sqrt{2\pi}} e^{-\frac{1}{2}\left(\frac{t-\mu}{\sigma}\right)^2} \Rightarrow (C_L)_{WC} = \frac{0.1\overline{\Delta C_L}T}{\sigma\sqrt{2\pi}} e^{-\frac{1}{2}\left(\frac{t-\mu}{\sigma}\right)^2}, \sigma = 2\mu^*T/6$$

$$(C_L)_{WC} = \frac{0.1T\overline{\Delta C_L}}{\frac{2\mu^*T}{6}\sqrt{2\pi}} e^{-\frac{1}{2}\left(\frac{t-\mu^*T}{\frac{2\mu^*T}{6}}\right)^2} = \frac{0.3\overline{\Delta C_L}}{\mu^*\sqrt{2\pi}} e^{-\frac{1}{2}\left(\frac{t-\mu^*T}{\frac{2\mu^*T}{6}}\right)^2} = \frac{0.3\overline{\Delta C_L}}{\mu^*\sqrt{2\pi}} e^{-\frac{1}{2}\left(\frac{3(t-\mu^*T)}{\mu^*T}\right)^2} \Rightarrow$$

$$(C_L)_{WC} = \frac{0.3\overline{\Delta C_L}}{\mu^*\sqrt{2\pi}} e^{-\frac{1}{2}\left(\frac{3(t-\mu^*T)}{\mu^*T}\right)^2} = \frac{0.3\overline{\Delta C_L}}{\mu^*\sqrt{2\pi}} e^{-\frac{1}{2}\left(\frac{3(t^*T-\mu^*T)}{\mu^*T}\right)^2} \quad (23)$$

$$(C_D)_{WC} = \frac{0.3\overline{\Delta C_D}}{\mu^*\sqrt{2\pi}} e^{-\frac{1}{2}\left(\frac{3(t-\mu^*T)}{\mu^*T}\right)^2} = \frac{0.3\overline{\Delta C_D}}{\mu^*\sqrt{2\pi}} e^{-\frac{1}{2}\left(\frac{3(t^*T-\mu^*T)}{\mu^*T}\right)^2} \quad (24)$$

$$\overline{\Delta C_L} = 0.94839 - 0.195478\exp(-0.00234646Re) - 7.9318\Delta\tau_D + 19.6205{\Delta\tau_D}^2 \quad (17)$$

$$\overline{\Delta C_D} = 0.903189 - 0.0356281\exp(-0.00027928Re) - 7.18999\Delta\tau_D + 17.7339{\Delta\tau_D}^2 \quad (18)$$

$$\mu^* = 0.04195 - 0.002684\ln(Re) + 0.2236\Delta\tau_A \quad (19)$$

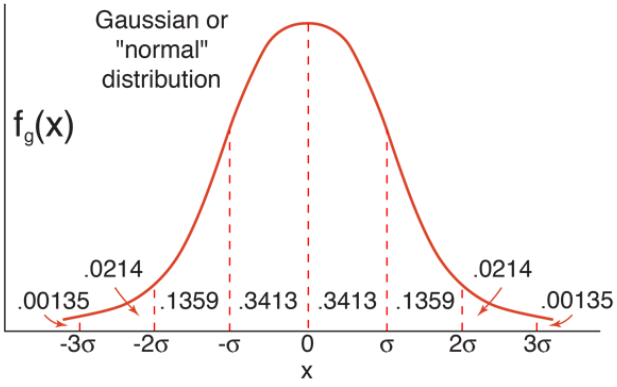

Fig.22: General normal distribution plot for of average value equal to unit. This function usually distributes the average value in the range of -3σ to 3σ

7-3- The results of the instantaneous lift and darg wake capture force coefficients

According to the algorithm in Figure 4, relations 23 and 24 for $(C_L)_{WC}$ and $(C_D)_{WC}$ are added to the blade element theory, and validation is performed in the current section. The results of the executions of Taguchi array numbers 4 and 16, as well as the verification executions V2 and V3, are shown in figures 23 and 24. It is evident from these figures that the normal distribution function has been applied correctly and that the effect of the blade element theory model of wake capture in both lift and drag coefficient is properly compatible with the CFD wake capture effect. An examination of the blade element theory without the effect of wake capture reveals that the force coefficients, in this case, agree well with the corresponding CFD force coefficients in the first cycle. Because the wing is moved from rest in the first cycle and there is no wake capture, matching this trend is logical for the coefficients. However, a comparison of the blade element theory lift and drag coefficients with wake capture, as well as the results of the 10th cycle of CFD, reveals that the trend of the force coefficients with the addition of this effect is very similar. This similarity first demonstrates that implementing wake capture terms into blade element theory by relations 23 and 24 improves the prediction of lift and drag force coefficients. As can be seen, using the blade element theory without the effect of wake capture does not cover the initial peak of the force coefficient at the beginning of the half cycle that can be seen in CFD, but by including the wake capture model, it is observed that this initial peak in the blade element theory results is taken into account. Second, the general similarity of the trend of force coefficients in CFD and the blade element theory over the entire half cycle indicates that the combination of translational force, rotational force, added mass force, and finally the wake capture model has the capability of precisely modelling the complex unsteady aerodynamics of the flapping wings.

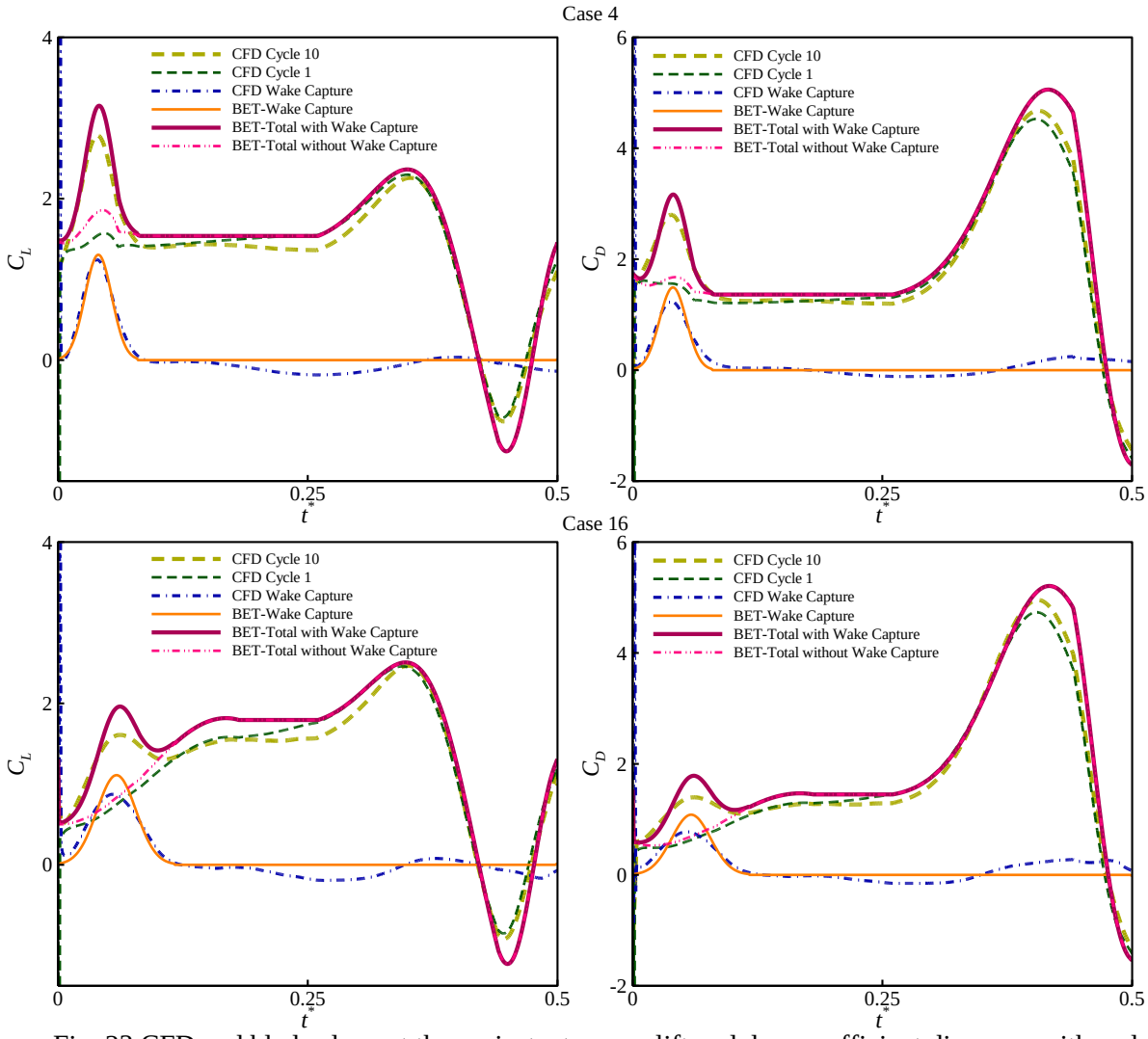

Fig. 23 CFD and blade element theory instantaneous lift and drag coefficient diagrams with and without wake capture effect in cases No. 4 and 16

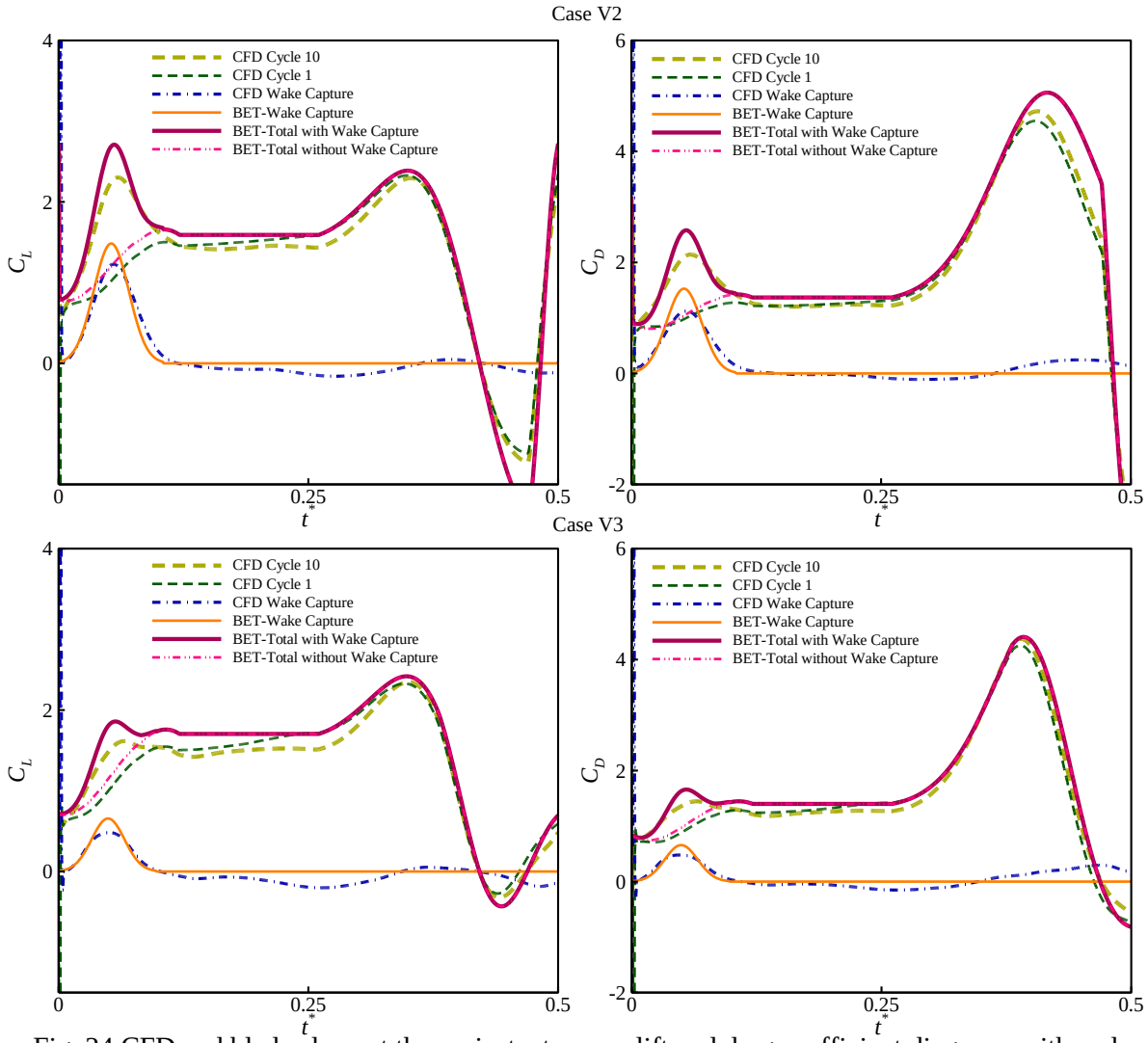

Fig. 24 CFD and blade element theory instantaneous lift and drag coefficient diagrams with and without wake capture effect in verification cases V2 and V3

7-4 Review of flow physics

As previously stated, wake capture is an aerodynamic phenomenon in which the position of wake vortices influences the amount of captured force. The Q criterion [19] is one of the parameters used to check different vortices in the sequence. This parameter indicates the presence of a vortex by demonstrating the dominance of vorticity over strain rate. Figure 25 depicts an appropriate level of the condition Q value to reveal the vortices at two points: t^*=9.00, which corresponds to the end of the ninth cycle (beginning of the tenth cycle), and t^*=9.05. The remaining sequences in the old and new cycles are represented by old and new symbols for the leading-edge vortex (LEV), trailing edge vortex (TEV), wing tip vortex (TV), and wing root vortex (RV). As seen, the wing collides with the vortices left in its wake at the start of the new half-cycle (t^*=9.05), resulting in the effect of capturing the wake.

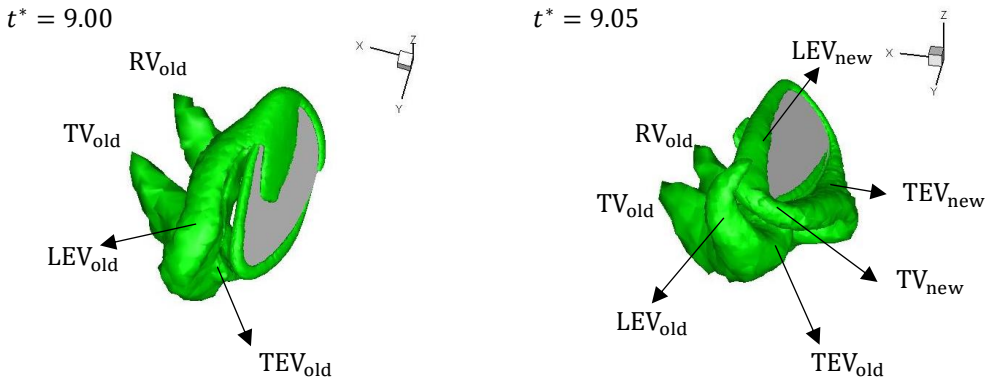

Figure 25. Levels of the same value of Q at the beginning of the flapping cycle and the position of different vortices in the wake

Figure 26 compares the levels of the same value of Q=2 over a full half cycle, corresponding to the first and tenth cycles at the same time. As is well known, the first cycle begins in a stationary state with no vortices in the fluid flow, and as the wing moves in this cycle, different vortices are produced. At t*=0.25, for example, the leading-edge vortex is dominant. The simultaneous examination of the first and tenth cycles reveals that the vortices are almost identical after the beginning of the half-cycles. This means that, except for the beginning of the half-cycle, when the effects of the previous cycle are present, the vortices of the first and tenth cycles are similar the rest of the time.

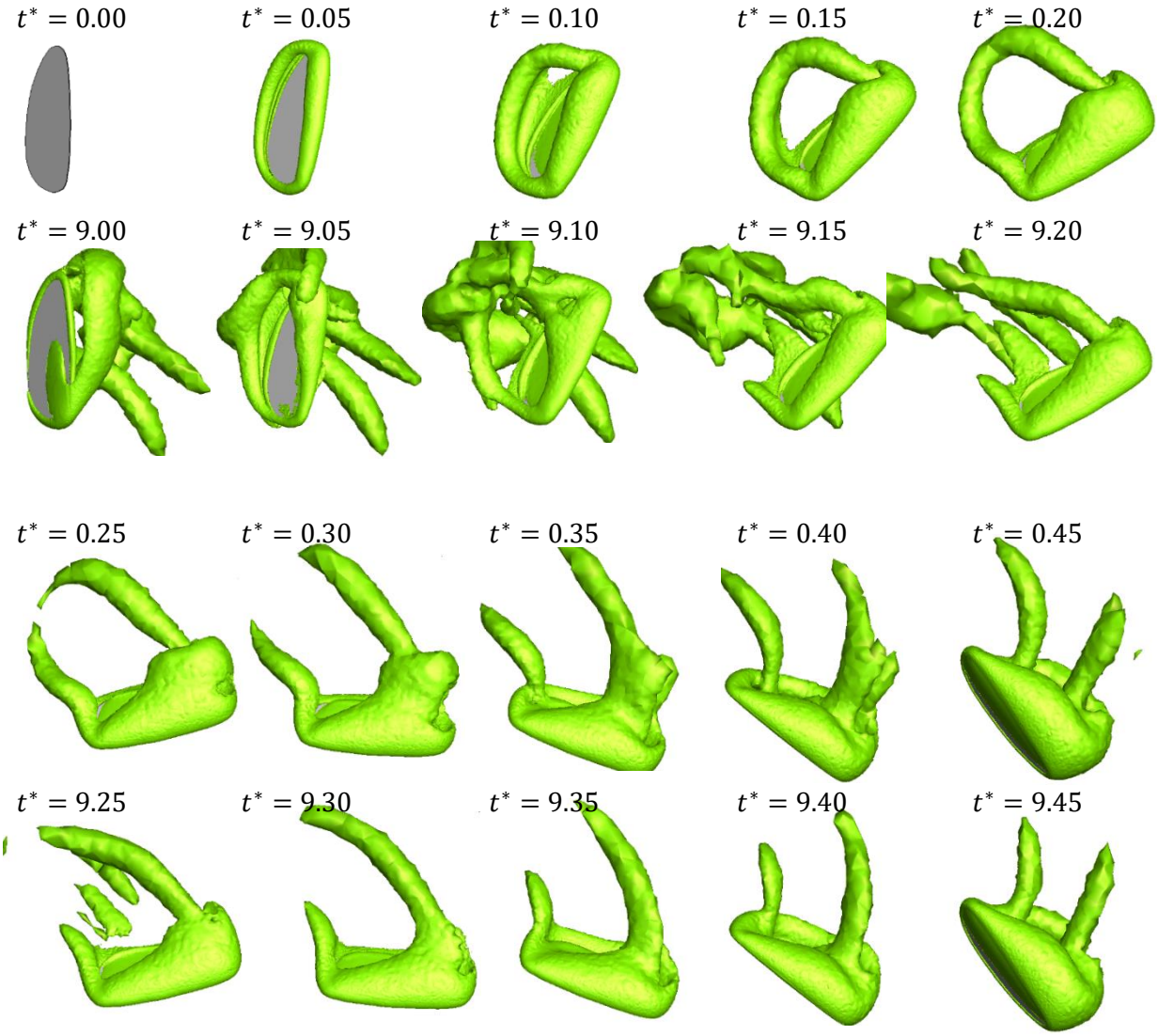

Figure 26. Levels of the same value of Q=2 in a half-cycle of flapping at the corresponding times of the first cycle and the tenth cycle.

8-**Conclusion**

As previously stated, researchers have favored the use of blade element theory as a quick method for simulating unsteady motions. However, no relations for the coefficients of the instantaneous lift and drag force coefficients at the start of the half cycle caused by the previous cycle's wake (wake capture) have been presented until now. Wake capture has, of course, been studied for some specific tasks, such as simple harmonic motions for applications in quasi-steady simulation. According to previous studies, the acceleration times of the wing at the beginning and end of the half cycle, as well as the Reynolds number, are three of the most important parameters in simulating the wake effect. As a result, in this study, a Taguchi orthogonal array of three parameters for computational fluid dynamics simulation was used: the dimensionless time of wing acceleration at the beginning of the half cycle, the dimensionless time of wing acceleration at the end of the half cycle, and the Reynolds number. Following that, the

average lift and drag wake capture coefficients at the start of the half cycle, as well as the dimensionless time when the maximum of these coefficients occurred, were calculated. Finally, a model for these output parameters based on the input parameters was obtained using the regression method. Finally, under the assumption of normal distribution, these models are placed in an instantaneous normal distribution function, and the relationships for instantaneous wake capture coefficient are extracted for use in the quasi-steady blade element theory. Examining the verification cases of the application of these wake capture relationships in the blade element theory, as well as the effects of translational force, rotational force, and added mass force, revealed that this developed theory is capable of correctly predicting the initial peak of the wake capture force. A qualitative examination of the lift and drag force coefficients in a half cycle reveals that the force coefficient trend in the blade element theory results is similar to the CFD results. This demonstrates an important result: this theory, which consists of four parts: transnational, rotational, added mass, and wake capture, adequately covers the general physics of these complex movements and can be widely applied. However, based on the current work's investigation of three input parameters on wake capture, it is suggested that other geometrical and motion parameters be investigated for a more complete improvement of this theory for wake capture.

9-References

.١ Dickinson, M.H., Lehmann, F.O. and Sane S.P., *Wing rotation and the aerodynamic basis of insect flight.* Science, 1999. **284** (5422): p. 1954-1960.

.٢ Keennon, M., Klingebiel K. and Won H. *Development of the nano hummingbird: A tailless flapping wing micro air vehicle*. in *AIAA aerospace sciences meeting*. 2012. AIAA Reston, VA.

.٣ Ellington, C.P., *The aerodynamics of hovering insect flight. I. The quasi-steady analysis.* Philosophical Transactions of the Royal Society of London. B, Biological Sciences, 1984. **305**(1122): p. 1.١٥-

.٤ Sane, S.P. and Dickinson M.H., *The aerodynamic effects of wing rotation and a revised quasi-steady model of flapping flight.* Journal of Experimental Biology, 2002. **205**(8): p. 1087-1096.

.٥ Li, Z.Y., Feng L., Kissing J., Tropea C. and Wang J., *Experimental investigation on the leading-edge vortex formation and detachment mechanism of a pitching and plunging plate.* Journal of Fluid Mechanics, 2020. **901**. 10.1017/jfm.2020.509

.٦ Han, J.S., Kim J.K., Won chang J. and Han J.H., *An improved quasi-steady aerodynamic model for insect wings that considers movement of the center of pressure* .Bioinspiration and Biomimetics, 2015. **10**.(٤) 10.1088/1748-3190/10/4/046014

.٧ Sun, M. and Tang J., *Unsteady aerodynamic force generation by a model fruit fly wing in flapping motion.* Journal of experimental biology, 2002. **205**(1): p. 55-70.

.٨ Nabawy, M.R. and Crowthe W.J., *A Quasi-Steady Lifting Line Theory for Insect-Like Hovering Flight.* PLoS One, 2015. **10**(8): p. e0134972.

.٩ Ellington, C.P., *The aerodynamics of hovering insect flight. V. A vortex theory.* Philosophical Transactions of the Royal Society of London. B, Biological Sciences, 1984. **305**(1122): p. 115-144.

.١٠ Truong, Q.T.,Nguyen Q.V., Truong V.T., Park H.C., Byun D.Y. and Goo N., *A modified blade element theory for estimation of forces generated by a beetle-mimicking flapping wing system.* Bioinspiration and Biomimetics, 2011. **6**.(٣) 10.1088/1748-3182/6/3/036008

.١١ Lee, Y.J., Lua KB, Lim TT and Yeo KS., *A quasi-steady aerodynamic model for flapping flight with improved adaptability.* Bioinspiration and Biomimetics, 2016. **11**.(٣) 10.1088/1748-3190/11/3/036005

.١٢ Wang, Q., Goosen J., and Van Keulen F., *A predictive quasi-steady model of aerodynamic loads on flapping wings.* Journal of Fluid Mechanics, 20 :٨٠٠ .١٦p. 688-719.

.۱۳ Hu, J., Xuan H., Yu Y. and Zhang J., *Improved quasi-steady aerodynamic model with the consideration of wake capture.* AIAA Journal, 2020. **58**(5): p. 2339-2346. 10.2514/1.J059015

.۱۴ Nabawy, M.R.A. and Crowther W.J., *On the quasi-steady aerodynamics of normal hovering flight part II: Model implementation and evaluation.* Journal of the Royal Society Interface, 2014. **11**.(۹۴)

.۱۵ Nabawy, M.R.A. and Crowther W.J., *On the quasi-steady aerodynamics of normal hovering flight part I: The induced power factor.* Journal of the Royal Society Interface, 2014. **11**.(۹۳)

.۱۶ Han, J.S., Chang J.W., Kim J.K. and Han J.H., *Role of trailing-edge vortices on the hawkmothlike flapping wing.* Journal of Aircraft, 2015. **52**(4): p. 1256-1266 10.2514/1.C032768.

.۱۷ Lentink, D. and Dickinson M.H., *Rotational accelerations stabilize leading edge vortices on revolving fly wings.* Journal of Experimental Biology, 2009. **212**(16): p. 2705-2719.

.۱۸ Ellington, C.P., et al., *Leading-edge vortices in insect flight.* Nature, 1996. **384**(6610): p. 626-630.

.۱۹ Lua, K., Lee Y.J., Lim T. and Yeo K., *Wing–Wake Interaction of Three-Dimensional Flapping Wings.* AIAA Journal, 2016. **55**(3): p. 729-739. 10.2514/1.J055214

.۲۰ Kim, H.-Y., Han J.S., and Han J.H., *Aerodynamic effects of deviating motion of flapping wings in hovering flight.* Bioinspiration & biomimetics, 2019.

.۲۱ Birch, J.M. and Dickinson M.H., *The influence of wing-wake interactions on the production of aerodynamic forces in flapping flight.* Journal of Experimental Biology, 2003. **206**(13): p. 2257-2272.

.۲۲ Wu, J. and Sun M., *The influence of the wake of a flapping wing on the production of aerodynamic forces.* Acta Mechanica Sinica, 2005. **21**(5): p. 411-418.

.۲۳ Chin, D.D. and Lentink D., *Flapping wing aerodynamics: From insects to vertebrates.* Journal of Experimental Biology, 2016. **219**(7): p. 920-932.

.۲۴ Young, J. and Lai J., *Oscillation frequency and amplitude effects on the wake of a plunging airfoil.* AIAA journal, 2004. **42**(10): p. 2042-2052.

.۲۵ Panah, A.E. and Buchholz J.H., *Parameter dependence of vortex interactions on a two-dimensional plunging plate.* Experiments in fluids, 2014. **55**(3 :(p. 1-19.

.۲۶ Addo-Akoto, R., Han J.S., and Han J.H., *Influence of aspect ratio on wing–wake interaction for flapping wing in hover.* Experiments in Fluids, 2019. **60**(11): p. 164.

.۲۷ Lehmann, F.O., *When wings touch wakes: understanding locomotor force control by wake–wing interference in insect wings.* Journal of Experimental Biology, 2008. **211**(2): p. 224-233.

.۲۸ Lee, Y. and Lua K., *Wing–wake interaction: comparison of 2D and 3D flapping wings in hover flight.* Bioinspiration & biomimetics, 2018. **13** :(۶)p. 066003.

.۲۹ Addo-Akoto, R., Han J.S., and Han J.H.. *Wing-Wake Interaction of Insect-Like Flapping Wing in Hover: Effect of Aspect Ratio and Kinematics at Re~ 104*. in *Fluids Engineering Division Summer Meeting*. 2019. American Society of Mechanical Engineers.

.۳۰ Lee, H., Jang J., and Lee S., *An investigation of kinematic parameters and stroke function on stroke reversal for three-dimensional vortex structures around a flapping insect wing.* European Journal of Mechanics-B/Fluids, 2020. **79**: p. 165-180.

.۳۱ Birch, J.M. and Dickinson M.H., *Spanwise flow and the attachment of the leading-edge vortex on insect wings.* Nature, 2001. **412**(6848): p. 729.

.۳۲ Ansari, S., Żbikowski R., and Knowles K., *Aerodynamic modelling of insect-like flapping flight for micro air vehicles.* Progress in Aerospace Sciences, 2006. **42**(2): p. 129-172.

.۳۳ Van Veen, W.G., Van Leeuwen J.L., and Muijres F.T., *A chordwise offset of the wing-pitch axis enhances rotational aerodynamic forces on insect wings: a numerical study*. Journal of the Royal Society Interface, 2019. **16**(155): p. 20190118.

.۳۴ Nakata, T., Liu H., and Bomphrey R.J., *A CFD-informed quasi-steady model of flapping-wing aerodynamics.* Journal of fluid mechanics, 2015. **783**: p. 323-343.

.۳۵ Rezaeiha, A., Montazeri H., and Blocken B., *On the accuracy of turbulence models for CFD simulations of vertical axis wind turbines.* Energy, 2019. **180**: p. 838-857.

.۳۶ Chanin, M.N., Kuei C.H., and Lin C., *Using Taguchi design, regression analysis and simulation to study maintenance float systems.* The International Journal Of Production Research, 1990. **28**(11): p. 1939-1953.

.٣٧ Zhang, H., Wen C., and Yang A., *Optimization of lift force for a bio-inspired flapping wing model in hovering flight.* International Journal of Micro Air Vehicles :(٢)٨ .٢٠١٦ ,p. 92-108.

.٣٨ Bao, Z., Yang F., Wu Z. Nyamsi N. and Zhang Z., *Optimal design of metal hydride reactors based on CFD–Taguchi combined method.* Energy Conversion and Management, 2013. **65**: p. 322-330. 10.1016/j.enconman.2012.07.027

.٣٩ Dsivaiah, P. and Chakradhar D., *Modeling and optimization of sustainable manufacturing process in machining of 17-4 PH stainless steel.* Measurement, 2019. **134**: p. 142-152.

.٤٠ Aguirre, T.G., Fuller L., Ingrole A., Seek T.W., Wheatley B.B., Steineman B.D., Donahua T.L.H. and Donahue S.W., *Bioinspired material architectures from bighorn sheep horncore velar bone for impact loading applications.* Scientific Reports :(١)١٠ .٢٠٢٠ ,p. 1-14.

.٤١ Chao, A., Chae Y., Changchuag X. and Lan Y., *Flutter and gust response analysis of a wing model including geometric nonlinearities based on a modified structural ROM.* Chinese Journal of Aeronautics, 2020. **33**(1): p. 48-63. 10.1016/j.cja.2019.07.006

.٤٢ Younes, B., *Modelling of the blend ratio effect on the mechanical properties of the biofibres.* The Journal of The Textile Institute, 2017. **108**(5): p. 692-702.

.٤٣ *mintab help*. Available from: https://support.minitab.com/en-us/minitab/19/help-and-how-to/statistical-modeling/regression/how-to/fit-regression-model/before-you-start/overview./

.٤٤ Archontoulis, S.V. and Miguez F.E., *Nonlinear regression models and applications in agricultural research.* Agronomy Journal, 2015. **107**(2): p. 786-798.